



### **Science Arts & Métiers (SAM)**

is an open access repository that collects the work of Arts et Métiers Institute of Technology researchers and makes it freely available over the web where possible.

This is an author-deposited version published in: <https://sam.ensam.eu>  
Handle ID: <http://hdl.handle.net/10985/18012>

#### **To cite this version :**

Yaroslav RAE, X. GUO, Nigel NEATE, Wei SUN, Adil BENAARBIA - On the microstructural evolution in 12% Cr turbine steel during low cycle fatigue at elevated temperature - Materials Science and Engineering: A - Vol. 773, p.138864 - 2020

Any correspondence concerning this service should be sent to the repository

Administrator : [scienceouverte@ensam.eu](mailto:scienceouverte@ensam.eu)



# On the microstructural evolution in 12% Cr turbine steel during low cycle fatigue at elevated temperature

Y. Rae<sup>a,\*</sup>, X. Guo<sup>a</sup>, A. Benaarbia<sup>b</sup>, N. Neate<sup>a</sup>, W. Sun<sup>a</sup>

<sup>a</sup>*Department of Mechanical, Materials and Manufacturing Engineering, University of Nottingham, Nottingham, Nottinghamshire, NG7 2RD, UK*

<sup>b</sup>*Arts et Métiers ParisTech, CNRS, Université de Lorraine, LEM3, F-57000 Metz, France*

---

## Abstract

In order to better understand the physical process of deformation and cyclic softening a 12% Cr martensitic stainless steel FV566 has been cyclically tested at high temperature in strain control. Increase in temperature was found to increase the cyclic life, softening rate and viscous stress magnitude. An increase in the dwell time led to the acceleration of the material degradation.

The microstructure changes and dominating deformation mechanisms were investigated by means of scanning electron microscopy, electron backscatter diffraction and transmission electron microscopy. The results have revealed a gradual sub-grain coarsening, transformation of lath structure into fine equiaxed subgrains, and misorientation angle development in blocks and packets until material failure. The softening behaviour was attributed to the mutual annihilation of the dislocations and rearrangement of the residual dislocation in the low energy structures.

*Keywords:* Low Cycle Fatigue, Cyclic Softening, Sub-Grain Coarsening, Annihilation of Dislocations, Martensite Reorientation

---

## 1. Introduction

Power generation is gradually transitioning from continuous to flexible operation due to a raise in intermittent renewable sources. The typical operating conditions for such materials consist of temperatures up to 600 °C and cyclic loadings comprising of repeated starts and stops. Subsequently, flexible operation leads to an increase in start-up and shut-down cycles resulting in premature failure and damage of power plant materials due to low cycle fatigue

---

\*Corresponding authors

(LCF). LCF damage occurs as a result of mechanical loads and sharp thermal gradients between the components' surface and the centre during thermomechanical cycling, when equipment is subjected to start-ups, shut-downs and power transients. Such damage gets further amplified by the presence of creep at high temperatures resulting in superimposition with damage from LCF (Fischer and Kuhn (2019a)). As the operational temperature increases, the deformation rate-dependency increases for the majority of power plant materials (Marahleh et al. (2006)). Consequently, this calls for an investigation into the potentially detrimental interactions between creep and LCF damages to ensure an improvement of operating conditions and better structural durability of power plant components. This study complements previous investigation by the authors of high temperature creep-fatigue interaction in FV566 alloy (Rae et al. (2019)).

Tempered lath martensite (Figure 1) is a small grain polycrystalline phase of steel; its structure comprises of prior austenitic grain (PAG) boundaries, packets and blocks (Zhao et al. (2019)). These blocks are divided into laths and subgrain regions, separated by low angle boundaries (LAB) formed by dislocation arrays. The densely distributed dislocation substructure within it resists plastic deformation by opposing the dislocation motion (O'Hara et al. (2017)). FV566 (X12CrNiMoV12-3) is a grade of martensitic steel commonly used within industrial steam and gas turbines, and was designed to be operated in high temperature and pressure environments (Smithells (2013)).

Classical strain controlled tests either with or without dwell periods are often performed to define the material properties (Saad et al. (2013); Benaarbia et al. (2018a)). A significant amount of information is available in the literature describing creep and fatigue behaviours of high chromium steels as well as creep-fatigue interaction and a good progress was done in interpreting the creep-fatigue data (Fournier et al. (2011); Benaarbia et al. (2018b)). The past research indicates two main observations common for high chromium steels undergoing low cycle fatigue at high temperatures: accelerated cyclic softening and decelerated stress relaxation behaviours (Zhang and Xuan (2017)). Martensitic steels, as well as some other small grain polycrystalline materials subjected to creep-fatigue loadings, are known to soften (Zhao et al. (2019); Jing et al. (2018); Wang et al. (2019); O'Hara et al. (2017)). Cyclic softening during strain

cycling has been attributed to the recovery process related to the LAB annihilation (Sauzay et al. (2005, 2008)). A number of authors have looked at mechanical performance of FV566 material at elevated temperatures (Chambers et al. (1991); Hyde and Chambers (1992); Perkins and Bache (2005); Turnbull and Zhou (2011)), as well as some other power plant materials (Holdsworth et al. (2007); Kupkovits and Neu (2010); O'Hara et al. (2017)), although only very limited information is available linking it to the changes in the microstructure.

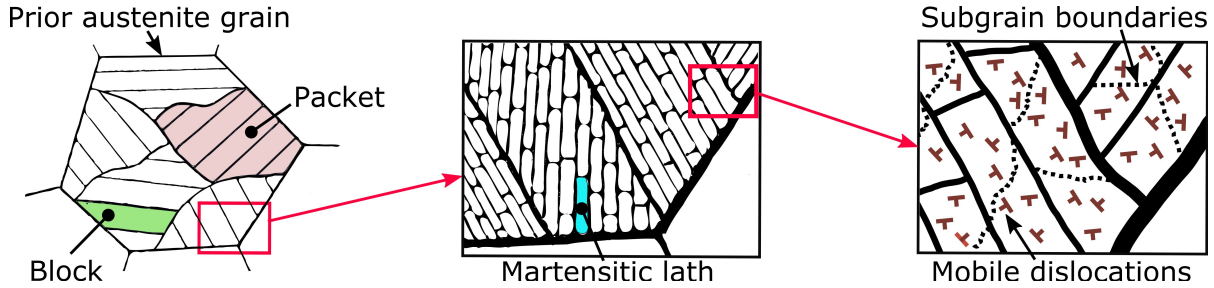


Figure 1: Schematic diagrams of martensitic hierarchical microstructure.

The present study incorporates a number of cyclic mechanical tests on FV566 steel using triangular waveform, with and without dwell periods, followed by microstructural characterisation. A few studies involving such loading patterns applied to similar materials are found in the literature (Li et al. (2019); Jing et al. (2018); Mishnev et al. (2015); Jürgens et al. (2019); Zhang et al. (2016); Fischer and Kuhn (2019a); Zhao et al. (2019); Batista et al. (2015)). A study carried out by (Wang et al. (2019)) using similar test patterns at 600 °C for a P92 steel alloy revealed that effective interaction between creep and LCF will have a strong combined effect on the material life and acceleration of microstructure evolution. The present study explores the relative roles of creep and LCF damage during such synergistic interactions through a series of tests carried out using different loading patterns and temperatures. The results are further characterised by conducting fracture surface and microstructure evolution investigations. Fracture surfaces for tensile, saw-tooth and dwell-type loading patterns are compared using optical and EBSD means. Microstructure evolution is studied by looking at grain structure and dislocations within it using EBSD and TEM techniques. In the present study, behaviour of martensitic 12% Cr FV566 steel was examined at temperatures of 300 °C and 600 °C. The influence of constant strain amplitude and variable length dwell period on the microstructure changes and LCF properties were



investigated to produce an improved understanding of the damage caused during operation. The characterisation includes the fatigue life, cyclic and tensile stress responses, followed by microstructure investigations of the initial, intermediate and failed states.

## 2. Material and experimental programme

The investigated steel alloy FV566 material was extracted from a location within a turbine rotor, near the centreline, where it was service-aged for approximately 90,000 hours at the temperature of around 420 °C and maximum speed of 3000rpm. The chemical composition of the material is as follows (wt.%): C-0.6; Si-0.038; Mn-0.668; Cr-11.9; Mo-1.68; Ni-2.52; V-0.298; S-0.006 and Fe-remainder. Cylindrical solid fatigue specimens (Figure 2a) with a gauge diameter of 5 mm and gauge length of 10 mm were made to ISO 12106 standard. The tests were carried out in air on Tinius Olsen H25KS electromechanical testing system fitted with a Tinius Olsen DSCCTOL 25 kN pancake style load cell and a Severn Thermal Solutions SF2107 split section resistance furnace. The temperature along the gauge length of the specimen was controlled using three thermocouples spaced out along the specimen surface. The strain was measured using a high temperature side-contact extensometer.

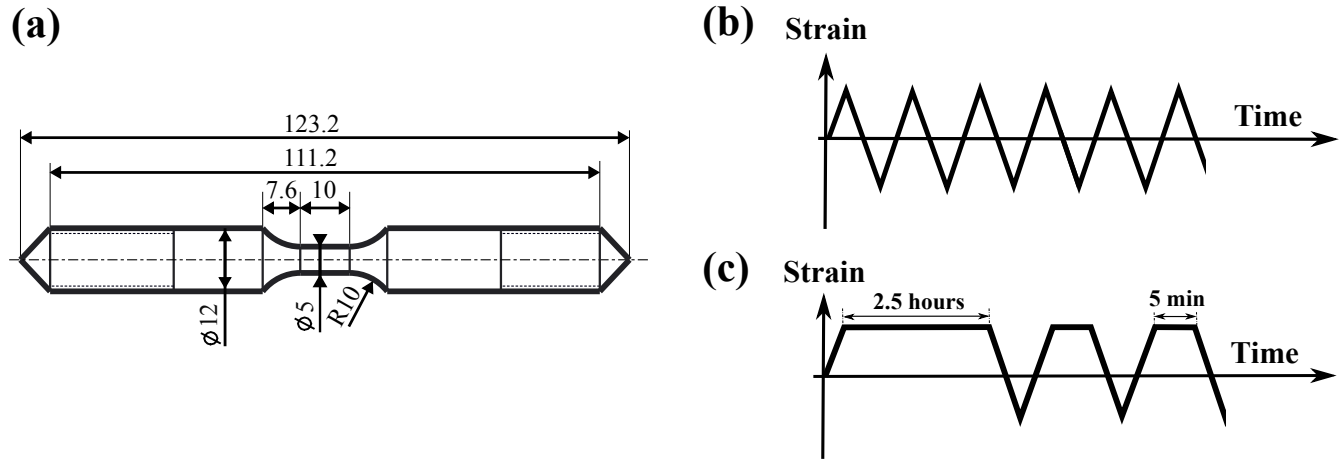


Figure 2: (a) Dimensions of the uniaxial round bar specimen (all measures given in mm). Schematic waveforms employed for (b) fatigue saw-tooth and (c) creep-fatigue dwell-type loading with tensile hold patterns.

A series of fully reversed LCF tests until failure and interrupted part way through, and a tensile test were carried out. The real loading pattern of an industrial gas turbine is complicated and it is very hard to completely replicate it experimentally. To try accurately predict material

properties, cyclic tests were done under idealised loading paths. The basis for such idealised tests is that the overall behaviour is a combination of the cyclic properties with rate dependent cyclic plasticity and temperature dependent creep. Due to the cyclic hardening, there is a combined visco-plasticity and creep-fatigue interaction is happening. The two given cyclic loading conditions were chosen to investigate the creep-fatigue behaviour. The strain controlled low cycle fatigue tests and creep-fatigue tests were conducted at temperatures of 300 °C and 600 °C under total strain control using saw-tooth and dwell-type waveforms with a constant strain rate of  $0.01 \text{ s}^{-1}$ . Test temperatures were chosen to cover an operational temperature range of rotating parts within a typical industrial gas turbine. All cyclic tests were performed under symmetrical push-pull conditions (load ratio  $R_\epsilon = -1$ ) and strain amplitudes of  $\pm 0.7 \%$ . A symmetrical triangular waveform was employed for the saw-tooth loading, and a trapezoidal waveform for the dwell type loading (Figure 2b-c). For dwell-type loading, the dwell period duration was imposed at the maximum tensile strain for a period of 2.5 hours for the first cycle and 5 min for all the following cycles. The dwell duration was chosen after careful investigation of the material stress relaxation times (the 5 min hold period was enough to reach the quasi-equilibrium state of the viscous stress). The data was acquired continuously until specimen fracture. Interrupted strain controlled LCF tests were performed at a temperature of 600 °C; the tests were stopped at zero load once the required number of cycles was reached. The monotonous tensile test was performed at a temperature of 600 °C and a strain rate of  $0.01 \text{ s}^{-1}$  until rupture. Prior to testing the gauge lengths of all specimens were ground and polished mechanically to avoid premature crack formation at the machined surfaces.

The material properties will be later used for visco-plasticity thermomechanical fatigue modelling. The model has two parts of parameters, a hardening part and a viscous part. Hardening parameters can be more accurately obtained by saw-tooth data, because hardening is the plasticity part. The dwell type test is a standard way of dealing with plasticity and viscous effects merged together. The loading needs some relaxation and the dwell period gives you a creep-fatigue interaction effect. Microstructure of the FV566 material was observed using SEM, EBSD and TEM techniques. Microstructures of the initial and ruptured states of

the investigated samples were characterised by means of a JEOL 7100F FEG-SEM scanning electron microscope. The SEM micrographs were captured using secondary electron imaging at an acceleration voltage of 15 kV. To obtain information regarding changes of grain sizes and orientations in the material during cyclic loading, electron backscatter diffraction (EBSD) characterisation was conducted using an Oxford instruments Aztec HKL system with Nordlys Max3 detector. Measurements were performed with step sizes ranging from 100 nm to 1.4  $\mu\text{m}$ . Misorientations of between 23-41° were designated as prior austenite grain boundaries. The samples for the EBSD investigations were cut parallel to the loading axis and prepared by conventional grinding and polishing steps, followed by final polishing using colloidal silica. The post-processing of the EBSD data and the generation of maps were conducted using the HKL Channel 5 software from Oxford Instruments. The post-processing included replacement of incorrectly indexed isolated points and filling of unindexed points which had at least 3 indexed neighbours, by extrapolation from neighbouring points. Typically less than 8% of the data points were unindexed. Transmission electron microscope images were acquired using a JEOL 2000FX TEM with incident electron beam voltage of 200 kV, a Gatan Orius digital camera, and a double-tilt eucentric sample holder. Lamellas for TEM were prepared by cutting and thinning slices from the bulk material using a focused ion beam FEI Quanta200 3D FIB-SEM machine. TEM results were then used to determine dislocation densities and widths of laths. Bright field images were captured in two beam condition to enhance dislocation contrast. Dislocations are typically not distributed continuously throughout the material (Butler (1969)), therefore location for dislocation density count was carefully chosen to be representative of a larger area and density was estimated by counting the individual dislocations within the grains. The width of the lath was found by calculating an average of 15 laths for each sample investigated.

### 3. Experimental results and discussion

The engineering stress-strain curve for tensile test data performed at 600 °C is presented in Figure 3. The basic mechanical properties extracted from the tensile curve have shown for material to exhibit a Young's modulus of 140 GPa, yield stress ( $\sigma_y$ ) of 420 MPa, ultimate tensile strength ( $\sigma_{UTS}$ ) of 456 MPa, elongation of 27% and area change of 90%. There is a hypothesis that

transient stress-strain behaviour can be estimated using  $\sigma_y$  and  $\sigma_{UTS}$  ratios (Halama et al. (2012)). A  $\sigma_{UTS}/\sigma_y$  ratio of 1.09 highlights a cyclic softening behaviour due to the low strain-hardening ability in tension.

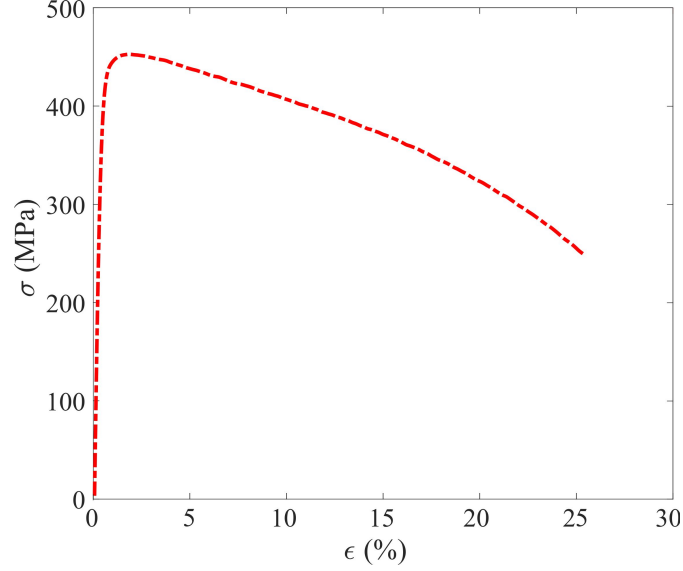


Figure 3: Tensile test of FV566 steel at 600 °C.

In order to illustrate the influence of the temperature and loading pattern on mechanical responses, Figure 4a-d shows the evolutions of the hysteresis loops at 300 °C and 600 °C for both saw-tooth and dwell-type loading waveforms. The hysteresis loops are plotted starting from the the 2nd cycle and finishing at approximately 90% of a total life. They are evenly spaced out by an equal fraction of stress drop to show the gradual shape evolution. Figure 4f presents the temperature and cyclic softening effect observed during the saw-tooth and dwell-type tests. A raise in temperature increases ductility, leading to a more significant drop in stress. Indeed, when the temperature increases from 300 °C to 600 °C the the fatigue life has increased by 43% for saw-tooth, and by 154% for dwell-type waveforms respectively. Moreover, the stress amplitude is decreasing as a function of a number of cycles highlighting cyclic softening. It can also be noticed that at the higher temperature, material exhibits considerably lower stress amplitudes at the beginning of the cyclic loading with a higher cyclic softening rate. Figure 4e demonstrates the stress relaxation during a strain hold. The reduction in stress during the 2.5 hour period was 66 MPa for 300 °C and 262 MPa for 600 °C. From this we can conclude that as the load is applied, the viscous stress magnitude is increasing with an increase in temperature. It can also

be observed that most of the viscous stress decrease is happening within the first few min with quasi-saturated state being reached within approximately 5 mins, after which the stress reaches quasi stabilised value. In terms of influence of the type of loading on cyclic life (Figure 4f), it can be observed that dwell-type loading brings a quicker degradation of the material, leading to a reduction of supported stress than saw-tooth loading at both investigated temperatures. The curves follow a general shape consisting of three distinct regions: a sharp first (I) initial softening regime, a second (II) region of stabilised softening rate, and a final third (III) region with a rapid drop that eventually culminates in fracture. In addition, the rate of stress drop in the third region becomes higher, indicating a softening rate increase, as the temperature is reduced. It may be noted that during the I and II stages of cyclic softening the SWT waveform has a higher average stress when compared to the DWT waveform at both 300°C and 600°C. During the III stage of cyclic softening at temperature of 600°C, both SWT and DWT waveforms produced similar values of the average stress at the correspond cycles. Previous investigations on a similar martensitic material MarBN (Benaarbia et al. (2020)) have shown a comparable trend during the III stage of cyclic softening.

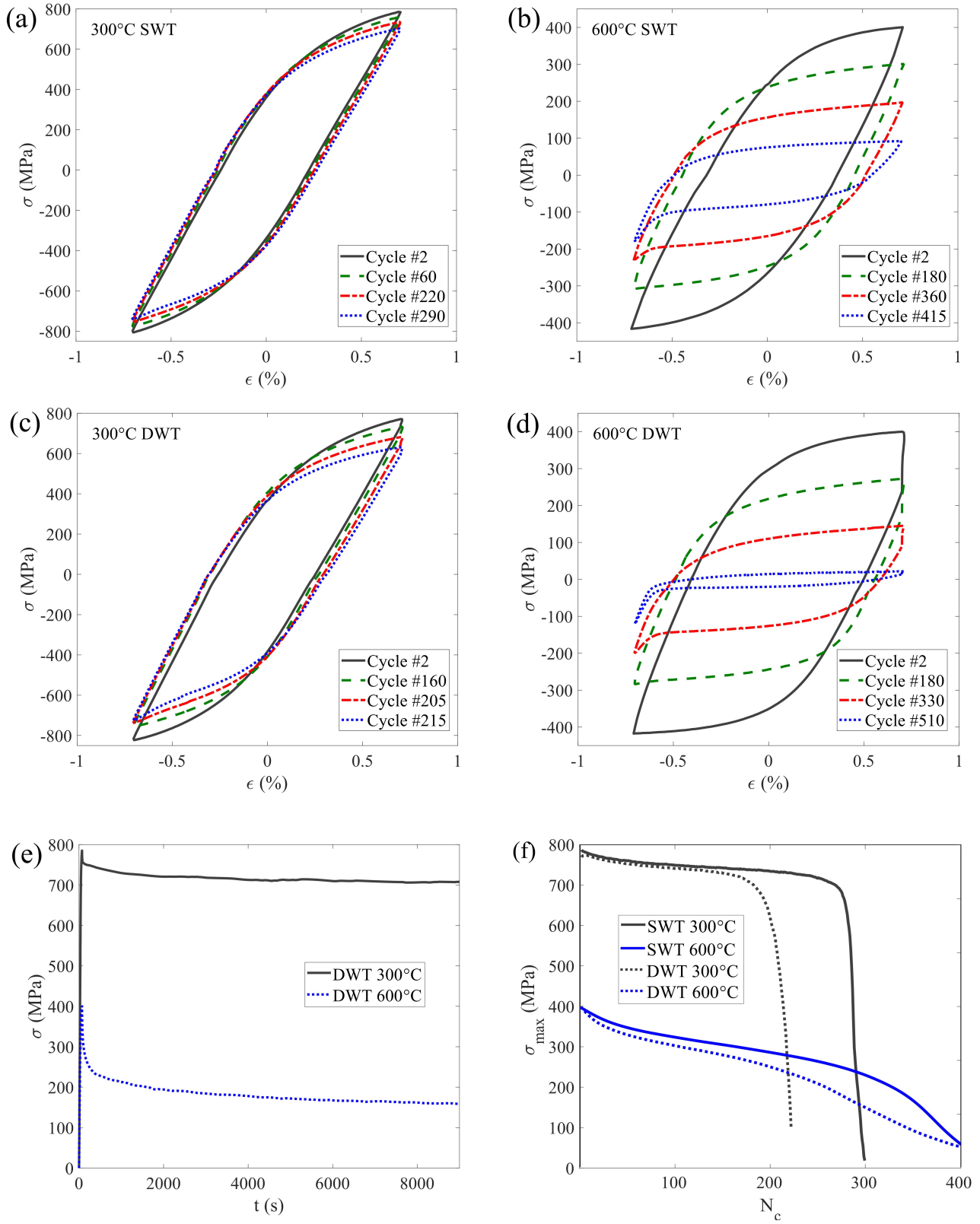


Figure 4: Change in stress-strain loops as the number of cycles increases for FV566 steel during saw-tooth (SWT) and dwell-type (DWT) waveforms at (a,c) 300°C and (b,d) 600°C. (e) Stress relaxation during 1st cycle of the selected dwell-type waveforms. (f) Maximum stress evolution.

From a macroscopic standpoint, materials subjected to cyclic loading are undergoing cyclic softening accompanied with noticeable evolution of grain size and dislocation density at the microstructure scale. This gives rise to the following questions. What role do grain size and dislocation density play during the cyclic softening? Is there an internal correlation between them? During the LCF test the stress curves shown a typical "S" softening shape. The softening process can be divided into three main stages: rapid softening in Stage I, saturation period in Stage II, and re-accelerated softening followed by a fracture in Stage III. Accordingly, different mechanisms could be responsible for the different stages of the cyclic softening, therefore supplementary investigations are needed in order to deeply investigate physical mechanisms of all softening stages.

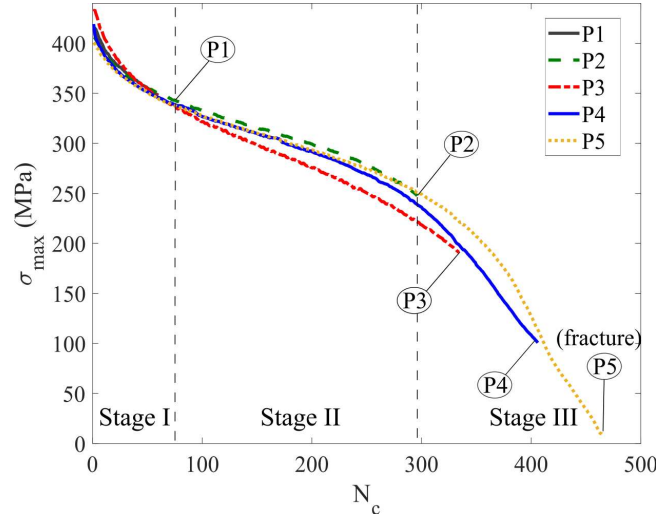


Figure 5: Cyclic behaviour during interrupted tests (P1-4) and until fracture (P5) for saw-tooth waveform at 600°C, highlighting the three stages of cyclic softening.

Interrupted tests were performed based on the conducted saw-tooth test at 600 °C. Stress evolutions for interrupted tests at 4 points (P1-P4) as well as results of a test conducted until failure (P5) are shown in Figure 5. Points P1 and P2 were located at the ends of Stage I and II respectively, while points P3 and P4 have been spaced out throughout the Stage III to give a more detailed information about this region. Although the softening rates slightly differ, the interrupted tests generally show a good repeatability.



## 4. Physical characterisation

### 4.1. Microstructure of as-received material

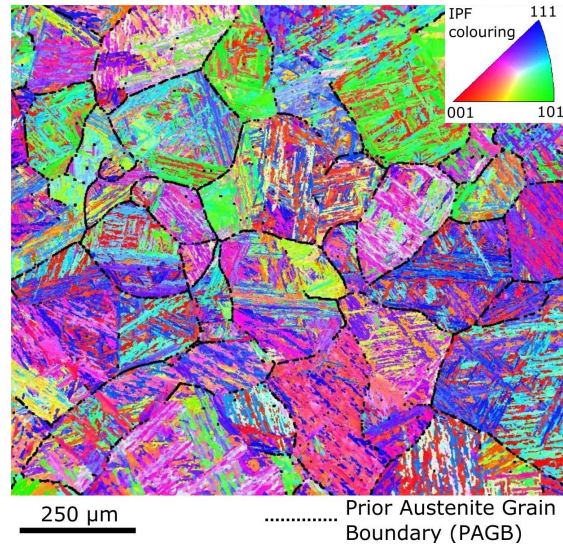


Figure 6: An EBSD orientation map of the as-received FV566 material providing an overview of the microstructure. The prior austenite grain boundaries are highlighted in black using 23-41° misorientation angles.

The high chromium content (near to 12%) in the FV566 steel and the unstable martensitic structure produced during quenching (from 900°C to 100 °C) contributes to the extremely high strength of the steel. To further improve the ductility, the steel is subsequently tempered at 650°C for 4 hours. As is well-known, static recovery of the unstable martensitic structure driven by the high elastic energy stored in the martensite proceeds during tempering. Although this recovery can result in the partial dislocation annihilation of opposite sign, thermally stable dislocation substructure cannot be formed during the short-term tempering. This means that static recovery of tempered martensitic structure inevitably occurs during the high-temperature service condition ([Ghassemi-Armaki et al. \(2009\)](#)). Meanwhile, different types of carbides precipitate at and within the supersaturated martensite grain boundary ([Seumangal \(2017\)](#)). After the heat treatment above, the steel exhibits a typical tempered martensitic structure with nano-sized precipitates and a high dislocation density. In the as-received material, several length scales, such as prior austenite grains (PAGs), packets, blocks, sub-blocks and laths, are involved. In terms of a Kurdjumov-Sachs orientation relationship ([Kitahara et al. \(2006\)](#)), PAGs, packets and blocks usually have the high-angle boundaries with a misorientation greater than



15°, whereas the sub-blocks and laths are low-angle boundaries (less than 15°). In the present study, Figure 6 shows that the PAGs in the as-received material are less than 300 μm in size with the misorientation in a range of 23-41°. Sub-blocks and laths have the average misorientation angles of 1.8° and 8.3°.

## 4.2. Fracture characteristics

### 4.2.1. Fractographic features

To understand the various fracture mechanisms under different loading conditions, fracture surfaces of the specimens failed under tensile, saw-tooth and dwell-type loadings were examined using SEM.

The deformation of the sample in pure tension (Figure 7a) produces a small fracture area due to necking that is caused by accumulation of the plastic flow. The fracture surface (Figure 7d) is rough in appearance and is covered by equiaxed shear dimples surrounded by a smooth shear lip which is expected in this type of ductile tensile-shear fracture resulting from microvoid coalescence.

In general, most materials subjected to LCF at high stresses have poorly defined Stage I (ASM (1987)). The largest portion of a crack growth is attributed to the Stage II and is happening via transgranular fracture. Compared with the fracture morphology of the tensile sample fatigue specimens with or without dwell time do not exhibit obvious dimples due to effect of the cyclic loading. Observations of the fracture surfaces show that the appearance of fatigue fracture also depends on the length of the dwell time. When the dwell time is zero, as in SWT test, two simultaneous cracks are developing (Figure 7b) that propagate perpendicularly to the loading direction, culminating in large final fracture that resulted from tension overload. The areas along the fatigue crack propagation had striations present typical to the ones resulting from the cyclic loading (Jing et al. (2018); Benaarbia et al. (2020)). From this, a conclusion can be made that the surrounding areas without the striations have formed during the final fracture, they have been marked as “Final fracture”. The regular equispaced fatigue striations (Figure 7e) resulted from an increased stress due to reduced cross-sectional area; they are smooth in appearance and not very well defined, possibly due to a high resistance of 12% Cr steel to oxidation. In case when dwell time is introduced as in DWT test (Figure 7c), a number of secondary cracks

are visible on the periphery of the gauge length. The main crack is propagating at an angle to the loading direction and the final fracture area is significantly smaller in size. The fatigue striations (Figure 7f) are very well defined and the valleys between the striations give rise to a large number of secondary cracks.

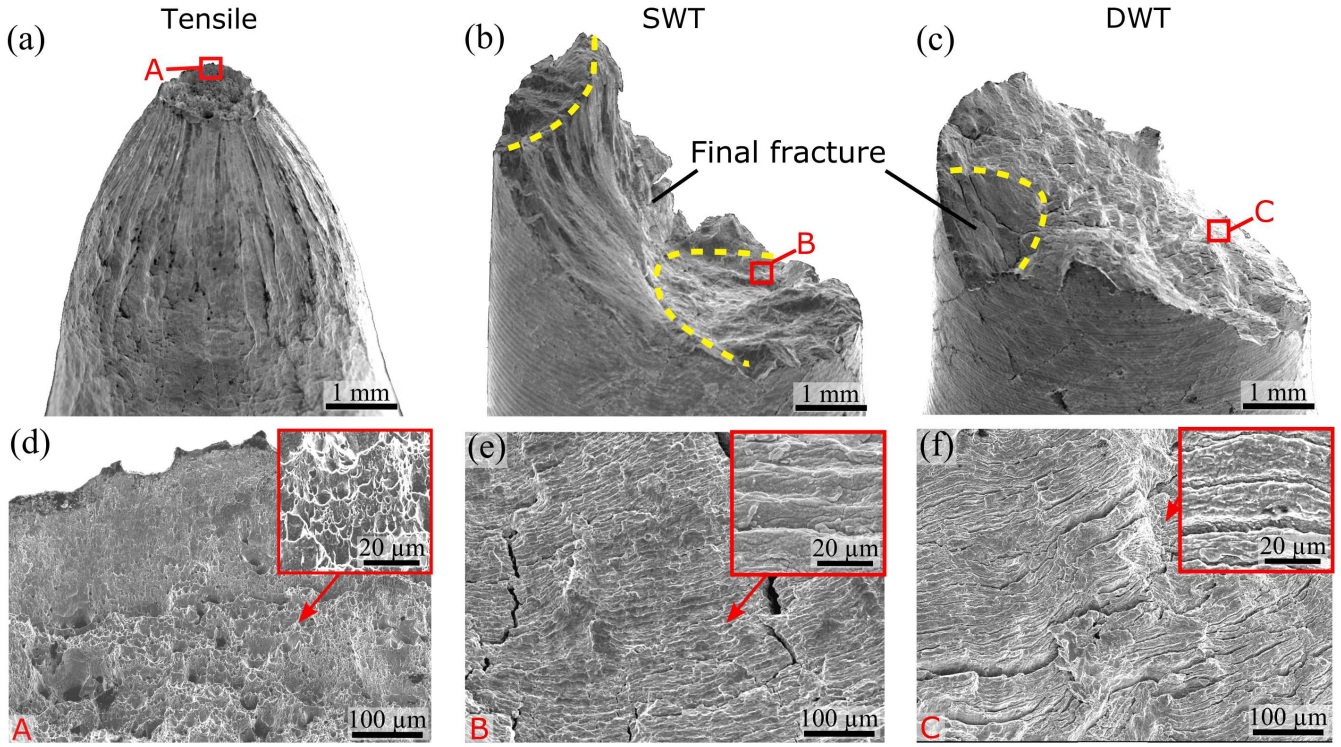


Figure 7: SEM micrographs of fractured samples (a-c) for FV566 steel tested at 600°C under tensile, saw-tooth and dwell-type loadings showing crack propagation, final fracture areas, and closer details (d-f) of the surface features and markings.

#### 4.2.2. Structure refinement

EBSD analysis was conducted on the tensile, saw-tooth and dwell-type failed specimens at the fracture surfaces. The fracture surfaces shown are approximately perpendicular to the loading direction during the cycling test. The exposure of steel to high temperature in air leads to the formation of the oxide scale on the surface which can be isolated using the EBSD technique (Higginson et al. (2006)). As shown in Figure 8, the microstructure refinement, when compared to the bulk of material away from the fracture surface, has been observed along the crack propagation routes for all three samples investigated. This is in line with the results by Higginson. The size of the grains within the oxide scale layer can be directly related to the size of the grains within the bulk of material. Based on the EBSD observation at the fracture surface and in order to investigate the annihilation of LAB's for FV566 steel under cyclic loadings, more

detailed EBSD analysis is focused on the zone away from the fracture area.

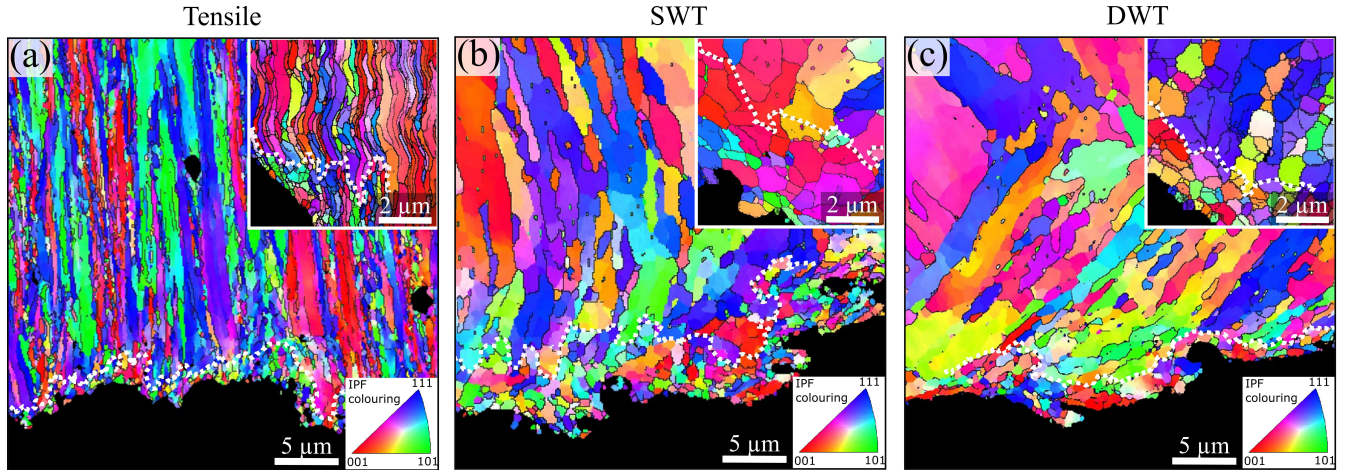


Figure 8: EBSD at fracture surface (grain boundaries are highlighted in black using 10-60° misorientation angles) and a higher magnification detail (highlighted using 1-60° misorientation angles) showing structure refinement of the samples near fracture areas under different loadings performed at 600°C using (a) Tensile, (b) Saw-Tooth and (c) Dwell-type loading patterns. The dotted white line follows the contour of the oxide scale.

#### 4.3. Microstructure evolution

##### 4.3.1. Annihilation of LABs

In order to study the microstructural evolution of the steel during the cyclic plastic deformation process, especially the laths and sub-blocks, EBSD maps of the samples interrupted at different lifetime fractions during 600°C saw-tooth test were created as shown in Figure 9. The point P0 was mapped on the as received material. For the interrupted samples P1-P4, the EBSD data was acquired in a location approximately half way between the tip of the dominant crack and the sample wall. The point P5 has been mapped on the fractured sample at a location in the close proximity to where the final cyclic growth of the dominant crack was occurring, just before the final fracture. The EBSD data is presented in terms of inverse pole figure (IPF) maps and intragrain misorientation angle (MA) maps positioned below. From the IPF maps it is possible to see that microstructure is getting more refined, as we move from P0 to P5, with grain boundaries getting closer together while some new smaller grains are being formed within the existing ones. Misorientation maps show the corresponding distribution of misorientation angles in the range of 0-5° across the lath and sub-block boundaries. When looking at P0, P1 and P2 we can see that the amount of blue on the map is increasing, indicating an increase in the low-angle boundaries. At P3 this is reversed and once we reach P5, the high density of red and yellow

indicates dominant presence of the high angle boundaries. From this we can conclude that average misorientation within grains decreases gradually up to the point when crack growth



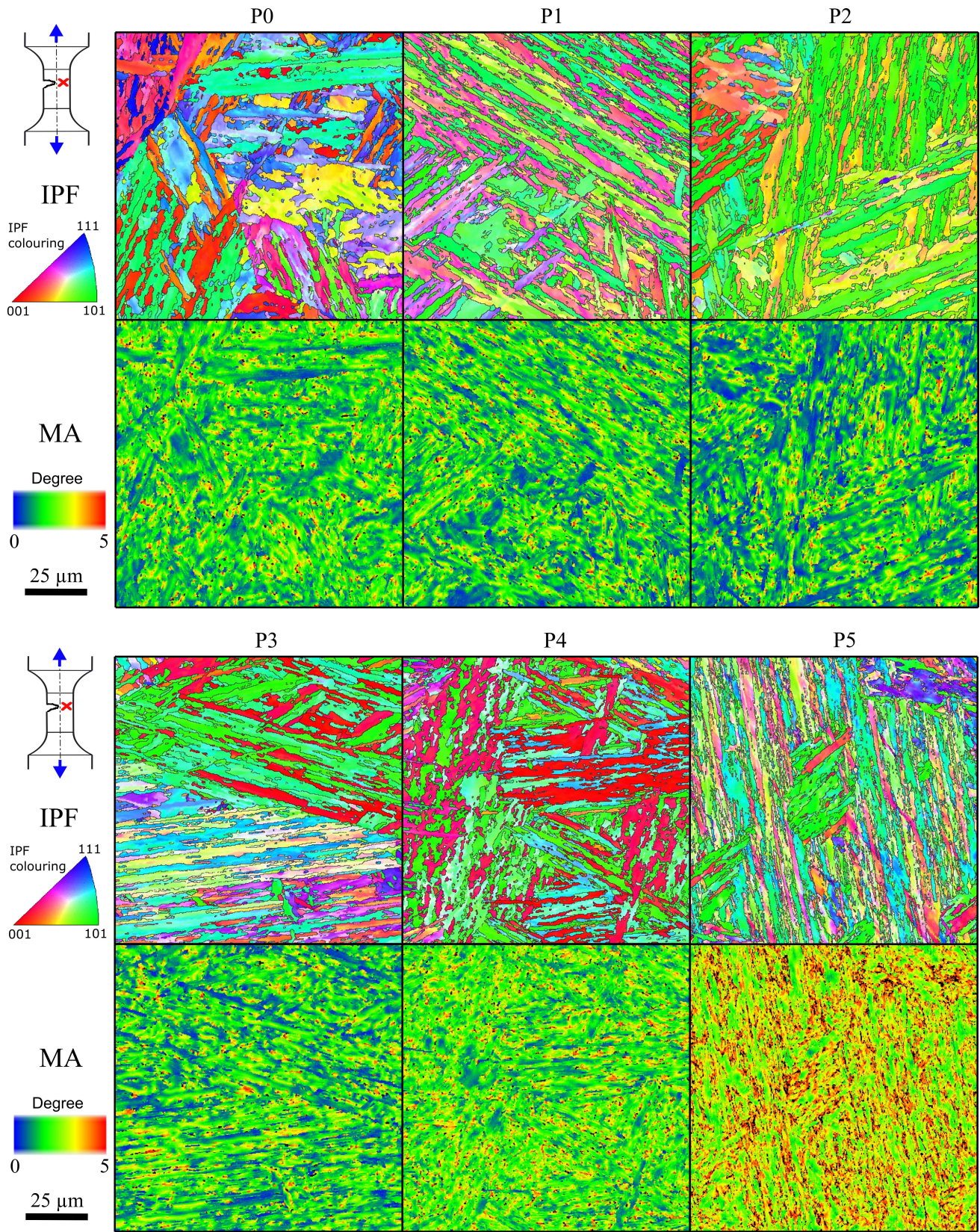


Figure 9: IPF (grain boundaries are highlighted in black using 10-60° misorientation angles) and intragrain MA - misorientation angle maps (rainbow scale: blue represents 0° misorientation from the reference pixel, red represents 10° misorientation from the reference pixel) for interrupted points P0-P5 during 600°C saw-tooth test. The EBSD map alignment corresponds to the orientation of the specimen during the test, as pictured in the loading schematic.



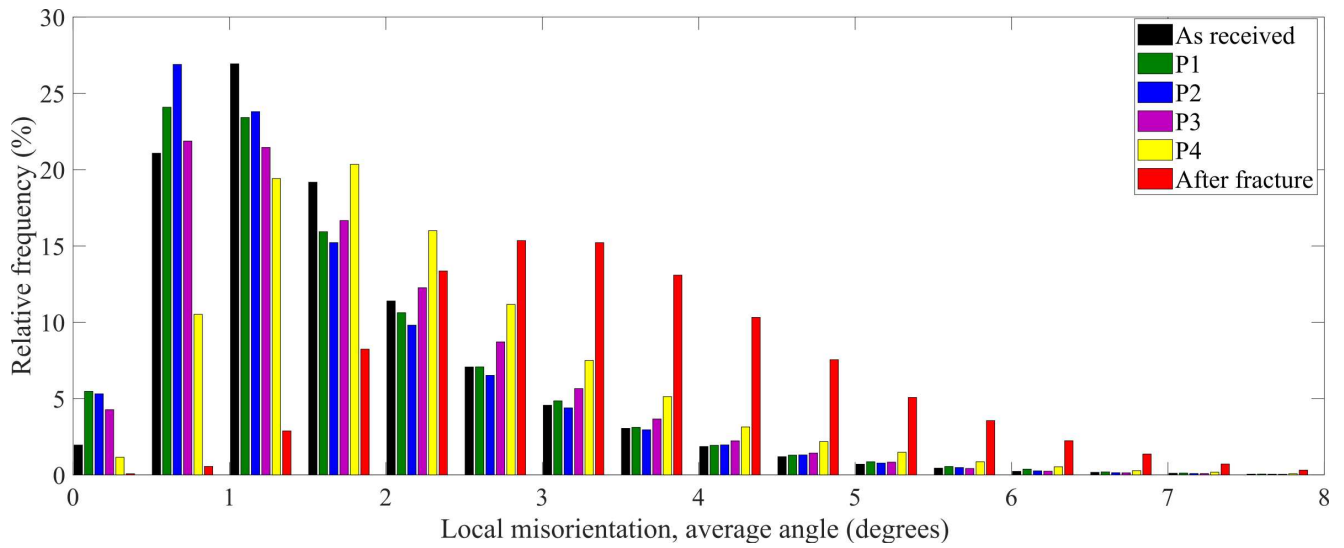


Figure 10: Misorientation angle statistical analysis of low angle boundaries at different number of cycles in saw-tooth test

accelerates. To investigate this further a more detailed analysis of misorientations was conducted.

The misorientation angle maps were used to create a bar chart shown in Figure 10 where the misorientation angle was limited to  $8^\circ$  to focus on LAB's. The presence of sub-block boundaries is visible at peaks between misorientations of approximately  $1.5^\circ$  to  $8^\circ$  in the as-received material. As the lifetime fraction is increased, these peaks gradually decrease in magnitude, whereas the frequency of lower angle boundaries starts to increase. This result is consistent with Huang's research (Huang et al. (2012)). As the cycle number continues to increase past point P2, the opposite is observed. It suggests the elimination of the sub-block structures during the cyclic plastic deformation process. This phenomenon is consistent with Sauzay's investigation (Sauzay (2009)). In the present study, this elimination of sub-block structures may be responsible for the dislocation glide during cyclic plastic deformation process. According to the study by Sauzay, if plastic slip system is activated during cyclic deformation process, mobile dislocations could be possibly moving to a dislocation with an opposite sign in the LAB which can result in the local dislocation annihilation and thereby the reduction of dislocation density and elimination of the sub-block structure. Additionally, owing to the knitting-out reaction, LAB dislocations can also interact with the mobile dislocations during deformation process. It can also contribute to the dissolution of sub-block boundaries.



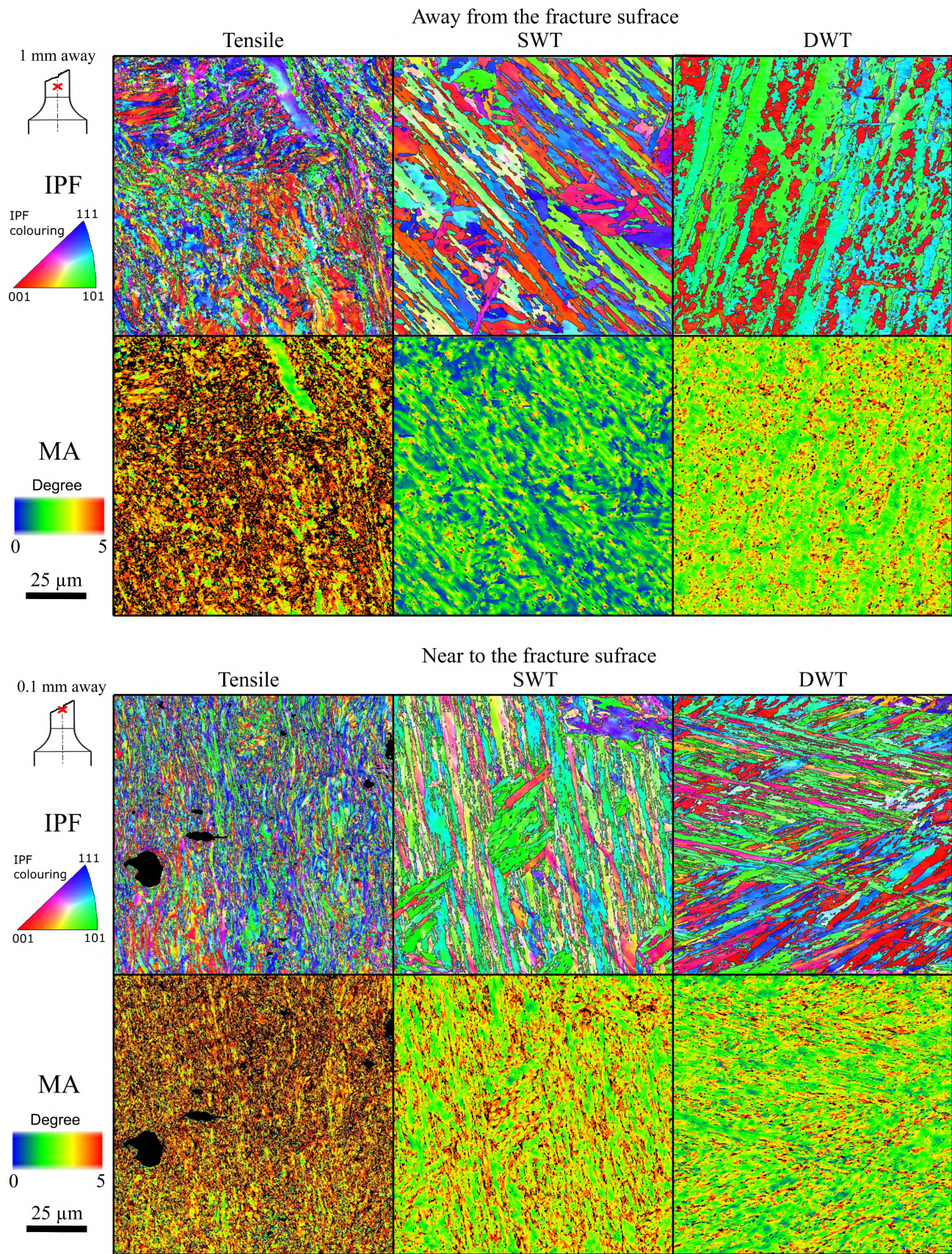


Figure 11: IPF (grain boundaries are highlighted in black using 10-60° misorientation angles) and intragrain MA - misorientation angle maps (rainbow scale: blue represents 0° misorientation from the reference pixel, red represents 10° misorientation from the reference pixel) for tensile, saw-tooth and dwell-type tests at locations near and away from the fracture surface.



The EBSD analysis results for the as received material, as well as, tensile, saw-tooth and dwell-type failed specimens close to (0.1 mm), and away (1 mm) from the fracture surfaces are shown in Figure 11 via IPF and misorientation maps. When compared to the as-received material (P0 in Figure 9), all three fractured samples demonstrate a level of refinement that increases closer to the rupture surface. In addition, the tensile sample shows that laths have been aligned along the loading direction due to presence of plastic flow.

#### 4.3.2. Transformation of the martensitic structure and the decrease of dislocation density

Figure 12 shows selected TEM micrographs of the specimens interrupted during saw-tooth test at various lifetime fractions. It can be seen from Figure 12 that FV566 steel in the as-received condition (Figure 12a) exhibits a pronounced tempered martensitic structure with the average lath width of approximately  $0.19 \mu\text{m}$ . Meanwhile, a high dislocation density (Figure 13a) and a large number of precipitates can also be observed both along and within subgrain boundaries. The initial dislocation density within the grain interiors was  $3.1 \times 10^{14} \text{m}^{-2}$ . As the lifetime fraction reaches point P1, although martensitic lath structure does not change significantly due a relatively small number of loading cycles completed at this stage, lath boundaries begin to vanish and dislocation density is reduced to  $1.4 \times 10^{14} \text{m}^{-2}$ , while lath width increases to  $0.37 \mu\text{m}$ . As the test progresses through point P2, the dislocation density reduces to  $1.1 \times 10^{14} \text{m}^{-2}$  and the lath width increases to  $0.61 \mu\text{m}$ . Moreover, some equiaxed subgrain structures in the localised regions can be observed in Figure 12c. As the number of cycles further increases, it can be seen from Figure 12d that the martensitic structure in the as-received condition is almost completely transformed into the equiaxed structure, in addition, the lath width becomes  $0.78 \mu\text{m}$  and the dislocation density reduces to  $0.3 \times 10^{14} \text{m}^{-2}$ . This phenomenon can be explained by the low energy dislocation structures (LEDS) hypothesis (Hansen and Hughes (1995)). During the deformation process of the material under cyclic loading, dislocation glide is the dominating mechanism. Generally, when compared with a random distribution of dislocations, the dislocation arrangement in a wall structure is favoured due to the decrease in the upper cut-off radius ( $R$ ) and thereby in the free energy per unit length of dislocation line ( $U_D^*$ ) (Huang et al. (2012); Hansen and Hughes (1995)). Based on this theory, martensitic



lath structure and sub-block structure are low-energy dislocation structures. Here,  $U_D^*$  can be expressed by the following equation:

$$U_D^* = \frac{Gb^2}{4\pi} f(\gamma) \ln\left(\frac{R}{b}\right) \quad (1)$$

where  $G$  is the shear modulus,  $b$  is the Burgers vector, and  $f(\gamma) = (1 - 0.5\gamma)/(1 - \gamma)$ .  $\gamma$  is Poisson ratio.

In this equation,  $R$  can be written by the general equation:

$$R = \frac{b}{\theta} \quad (2)$$

where  $\theta$  is the misorientation angle of the low-angle boundary. From this equation it can be seen that  $R$  is inversely proportional to  $\theta$ , and the increase of misorientation angle of the equiaxed structure can contribute to the reduction of  $U_D^*$ . Thus, at a given dislocation density, the transition of the original martensitic structure into equiaxed structure in the material will decrease  $U_D^*$  during the cyclic plastic deformation due to the dislocation reconfiguration. This provides a driving force for the microstructural transition. In general, the cyclic plastic deformation of the material has a significant effect on the total dislocation density ( $\rho$ ) and the total stored energy ( $U_D$ ) written by the following relationship:

$$U_D = \rho U_D^* \quad (3)$$

As observed in this study, cyclic plastic deformation results in the dislocation rearrangement and annihilation which causes the reduction of dislocation density in the material. According to the equation 3, the decrease of dislocation density will lead to the reduction of  $U_D$ .

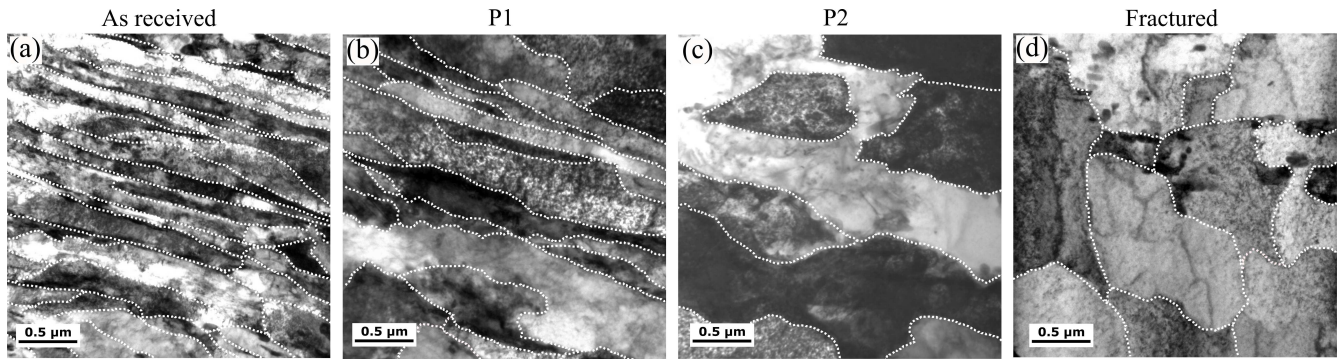


Figure 12: TEM observations of the as-received material, interrupted points P1-2 and fractured sample during the 600°C fatigue test showing subgrain size evolution. Dotted white lines highlight subgrain boundaries.

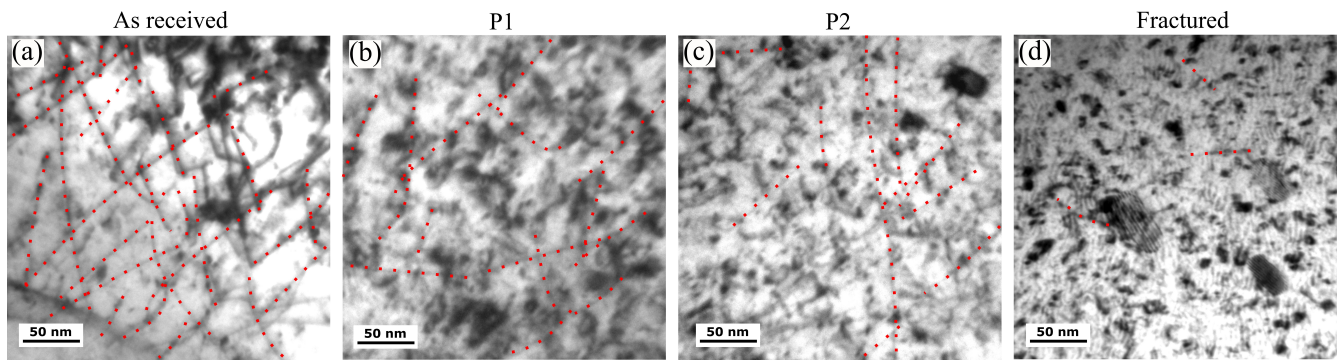


Figure 13: TEM bright field observations at two beam condition for the as received material, interrupted points P1-2 and fractured sample during the 600°C fatigue test showing dislocation structure within individual subgrains. Dotted red lines highlight dislocations.

In the current investigation, microstructure evolution, such as the reduction of dislocation density, elimination of sub-block structure and transition from martensitic structure into equiaxed structure can be observed during the cyclic plastic deformation process. All these changes in the microstructure may be attributed to the dislocation reconfiguration in the material which provides a driving force for the observed microstructure transition. Therefore, the essence of microstructural evolution under cyclic loading condition is the transition from unstable tempered martensitic structure into the low-energy equilibrium structure.

#### 4.3.3. Surface modification

As is mentioned above, microstructure evolution of the steel under cyclic loading at high temperature, such as the decrease of dislocation density, annihilation of LABs and transition from martensitic structure into equiaxed structure can be seen in this study. Additionally, fatigue accumulated damage can be expressed by specimen surface modification. In order to understand

crack initiation and propagation processes, the interrupted LCF tests performed at 600 °C were investigated using optical microscopy, as shown in Figure 14. It presents the typical cross-section optical micrographs of the as-received material and specimens at different damage stages. In the as-received material no cracks were observed prior to testing, as shown in Figure 14a. It can be seen from Figure 14b that the nucleation of a surface crack can be observed at the end of stage I which is about 10% of the original fatigue life. This finding is consistent with Ankur's result (Chauhan et al. (2017)). It can be concluded from the current observations that LCF is mainly dominated by the crack propagation and coalescence, since the microcracks nucleate quickly at the early stage of the test under cyclic loading. But it is worth noting that crack initiation is a complex phenomenon. Several factors, such as roughness of the sample's surface, local inclusion and other microstructural characteristics of the specimens, and the difference in the chemical composition can have an effect on the crack initiation, so it is difficult to remove the uncertainties of this issue. Generally, the nucleation of a surface crack under cyclic loading at high temperature can be attributed to the grain boundary slip during local cyclic plastic deformation. Once the crack initiates, it continues to propagate along the maximum shear stress plane, as shown in Figure 14c-e. It can be seen that crack propagation direction is at approximately 45° angle to the load direction in the stage I. Then the crack propagation direction is becoming perpendicular to the maximum principal stress and is at a 90° angle in the stage II. Finally, the crack propagates rapidly until its fracture. Note, that the surfaces of these cracks are also covered with oxide coating some of which had flaked off and that short cracks branching out from it were possibly oxide induced. Typically, cracks branch out to connect with non-metallic inclusions. In this study, the crack morphology under the LCF loading condition is characterised by the crack branching at the crack end, as can be observed from Figure 14d, and the crack has obvious oxidation characteristics. It indicates that the test temperature has a significant effect on crack propagation at 600°C. The high temperature leads to formation of a pronounced oxide layer on the surface of the steel. Because the tensile loading results in the crack to be in an open state during LCF test, stress field at the crack tip is able to promote oxygen diffusion. The opened crack zone is becoming a local preferential oxidation site. It will be further oxidised at the high-temperature

and the crack is branching out, so it continues to form a branched crack morphology. For the 9-12%Cr steels, several investigations have pointed out that the cracking of the oxide layer under LCF loading creates a favourable condition for the nucleation of fatigue cracks which is one of the reasons for the decrease of fatigue life ([Chauhan et al. \(2017\)](#); [Fischer and Kuhn \(2019b\)](#)). It can be observed from Figure 14b that the oxide layer of the specimen is formed at an early stage of the test, which is prior to 10% of original fatigue life. Since this brittle oxide layer gradually cracks and peels off during the LCF test, the surface oxide layer cannot hinder the penetration of oxygen into the material. The crack is re-exposed to the high-temperature environment. These cracked oxide layers can assist the nucleation of fatigue cracks, and also promote the propagation of fatigue cracks. Based on all these observations, the effect of high-temperature induced surface oxidation under LCF loading cannot be underestimated in the current study. The microcracks developed at different stages will directly change the stiffness of the specimens.

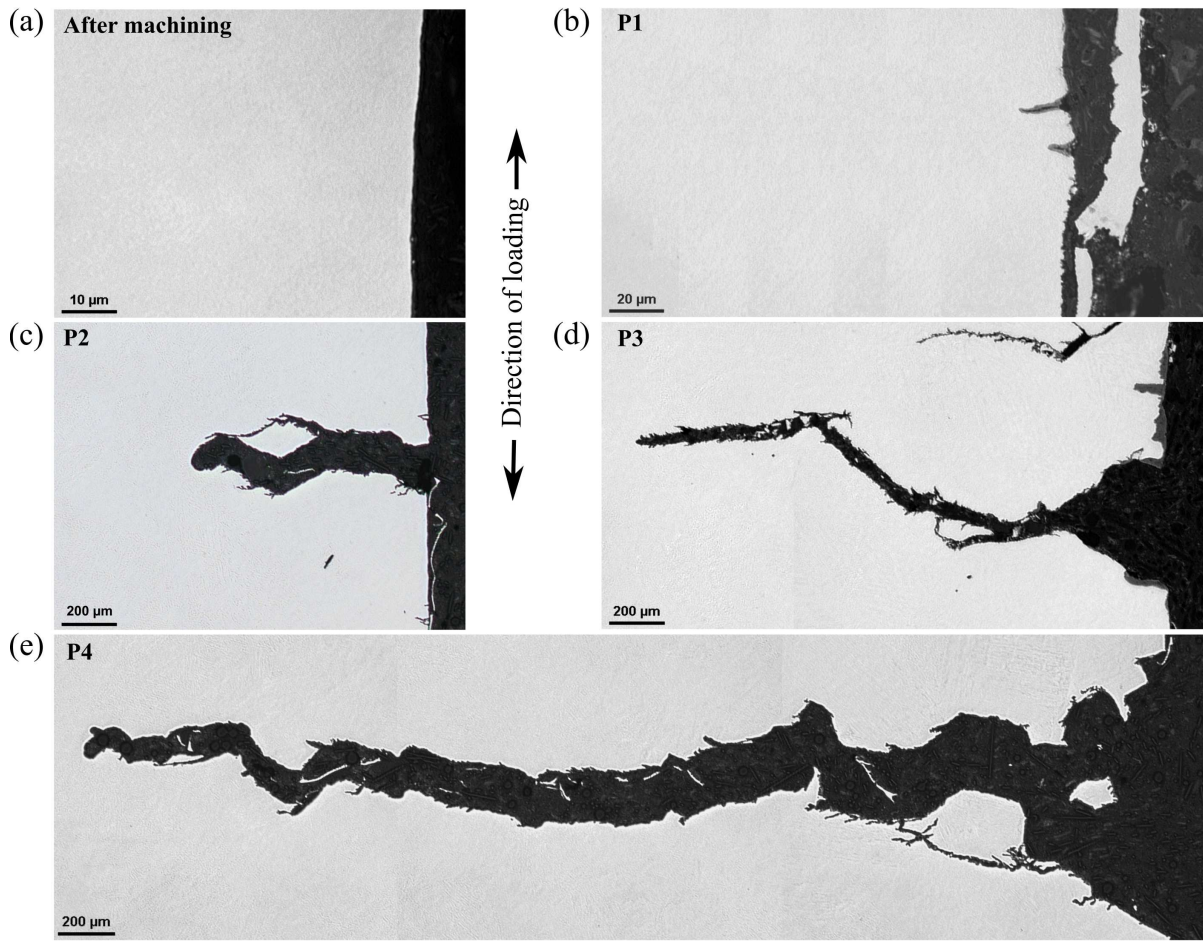


Figure 14: SEM micrographs at different magnifications of the gauge length cross section showing the (a) fatigue sample surface finish of the as received material after machining and before the test and (b-e) crack size initiation and evolution through the fatigue sample at interrupted points P1-4 during the fatigue test performed under saw-tooth loading at 600 °C

#### 4.4. Cyclic softening mechanisms

The material subjected to LCF loading and high temperature exhibits a significant cyclic softening which can be reasonably attributed to the microstructural evolution and surface modification. Microstructural evolution of the steel under cyclic loading (Figure 15), such as the decrease of dislocation density, annihilation of LABs and transition from the martensitic structure into the equiaxed structure can be observed in the current investigation. Definitely, this microstructure modification is dependent on the cyclic softening of the steel which was reported in the previous investigation (Rae et al. (2019)). In addition to the microstructural evolution, some local micro-cracks and macro-cracks can also be observed during the cyclic plastic deformation of the material. In this study, it is worth noting that local micro-cracks can be detected at an early stage of the test which is only 10% of the original fatigue life. It implies that crack propagation



and coalescence under cyclic loading may play a significant role in the LCF process. Meanwhile, because stress field at crack tip is able to promote oxygen diffusion, crack propagation under cyclic loading can be assisted by the high-temperature oxidation. These factors all contribute to the cyclic softening of the steel. In the present investigation, microstructure degradation and surface modification may occur simultaneously during cyclic plastic deformation of the steel. It is difficult to separate the effect of both factors on the cyclic softening.

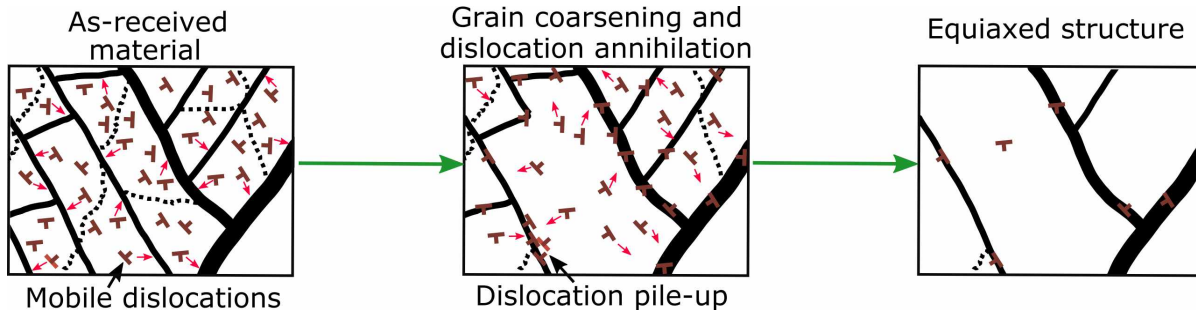


Figure 15: Schematic diagram of the microstructure of the as-received state and after cyclic loading.

## 5. Summary and conclusions

In order to evaluate the creep-fatigue fracture life of 12% Cr FV566 steel, a tensile and two types of LCF tests were carried out and effects of the temperature and hold time on fatigue life were investigated. Cyclic softening has been observed for both LCF loading types. At higher temperature material exhibited an increase in the viscous stress magnitude and a much higher softening rate. The cyclic life for both LCF loading types was found to increase with an increase in temperature. In terms of the loading type, an increase in the dwell time brought a quicker degradation of the material.

The misorientation within grains was evaluated using the EBSD intragrain misorientation maps. For all three loading types microstructure refinement has been observed along the crack propagation routes. In the interrupted samples misorientation angle development has shown that blocks and packets got more refined and sub-block structures were eliminated as the test progressed. This has lead to the dislocation glide during cyclic plastic deformation process. At the same time, the average grain misorientation angle was found to reduce during the I and II stages of fatigue, with a sharp increase in the final III stage.

TEM was employed to look at the laths. During the cyclic deformation the lath structure was found to transform to a fine equiaxed subgrain structure due to the dislocation's reconfiguration in the material, as it transitioned from an unstable tempered martensitic structure into the low-energy equilibrium structure. The cyclic softening effect was correlated to the coarsening of the initial martensitic laths into larger subgrains and to the reduction of the dislocation density. The subgrain size gradually increased from  $0.19\ \mu\text{m}$  at the beginning of the test to  $0.78\ \mu\text{m}$  after fracture. The grain coarsening of the martensitic grains was found to happen due to the rearrangement of low angle grain boundaries. During the cyclic deformations, the dislocation density was found to gradually change from  $1.4 \times 10^{14}\text{m}^{-2}$  at the beginning to  $0.3 \times 10^{14}\text{m}^{-2}$  after fracture due to annihilation of the dislocations. The process of dislocation annihilation has led to the decrease of the subgrain misorientations.

## 6. Acknowledgements

This work was supported by the Engineering and Physical Sciences Research Council UK (Grant numbers: EP/L016206/1, EP/N509991/1 and EP/K021095/1). The funding is provided through the EPSRC Centre for Doctoral Training in Innovative Metal Processing (IMPACT [impact.ac.uk](http://impact.ac.uk)), EPSRC/TSB IMPULSE project and EPSRC Flex-E-Plant project. The work was also partly sponsored by the RWE Generation (UK). The authors would also like to acknowledge RWE for permission to publish this paper.

The authors thank the Nanoscale and Microscale Research Centre (nmRC) at University of Nottingham for providing access to SEM, EBSD and TEM instrumentation, and Shane Maskill for conducting mechanical tests.

## 7. Data availability statement

The raw/processed data required to reproduce these findings cannot be shared at this time as the data also forms part of an ongoing study.

## 8. References

ASM, 1987. American Society for Metals Handbook: Fractography. Vol. 12.

- Batista, M., Marinelli, M., Hereñú, S., Alvarez-Armas, I., 2015. The role of microstructure in fatigue crack initiation of 9–12%Cr reduced activation ferritic–martensitic steel. *International Journal of Fatigue* 72, 75 – 79.
- Benaarbia, A., Rouse, J., Sun, W., 2018a. A thermodynamically-based viscoelastic-viscoplastic model for the high temperature cyclic behaviour of 9–12% Cr steels. *International Journal of Plasticity* 107, 100 – 121.
- Benaarbia, A., Xu, X., Sun, W., Becker, A., Jepson, M. A., 2018b. Investigation of short-term creep deformation mechanisms in MarBN steel at elevated temperatures. *Materials Science and Engineering: A* 734, 491 – 505.
- Benaarbia, A., Xu, X., Sun, W., Becker, A., Osgerby, S., 2020. Characterization of cyclic behavior, deformation mechanisms, and microstructural evolution of marbn steels under high temperature conditions. *International Journal of Fatigue* 131, 105270.  
URL <http://www.sciencedirect.com/science/article/pii/S0142112319303743>
- Butler, T., 1969. On the determination of dislocation densities. Vol. E-69-1. United States Naval Academy Engineering Department: Annapolis, Maryland.
- Chambers, A., Hyde, T., Webster, J., 1991. Mixed mode fatigue crack growth at 550°C under plane stress conditions in Jethete M152. *Engineering Fracture Mechanics* 39 (3), 603 – 619.
- Chauhan, A., Hoffmann, J., Litvinov, D., Aktaa, J., 2017. High-temperature low-cycle fatigue behavior of a 9Cr-ODS steel: Part 1 - pure fatigue, microstructure evolution and damage characteristics. *Materials Science and Engineering A* 707, 207–220.
- Fischer, T., Kuhn, B., 2019a. Impact of frequency, hold time and atmosphere on creep-fatigue of a 9–12% Cr steel from 300 °C–600 °C. *International Journal of Fatigue* 124, 288 – 302.
- Fischer, T., Kuhn, B., 2019b. Influence of steam atmosphere on the crack propagation behavior of a 9–12% Cr ferritic/martensitic steel at temperatures from 300 °C to 600 °C depending on frequency and hold time. *International Journal of Fatigue* 119, 62 – 77.



- Fournier, B., Dalle, F., Sauzay, M., Longour, J., Salvi, M., Caës, C., Tournié, I., Giroux, P.-F., Kim, S.-H., 2011. Comparison of various 9–12%Cr steels under fatigue and creep-fatigue loadings at high temperature. *Materials Science and Engineering: A* 528 (22), 6934 – 6945.
- Ghassemi-Armaki, H., Chen, R., Maruyama, K., Yoshizawa, M., Igarashi, M., 2009. Static recovery of tempered lath martensite microstructures during long-term aging in 9–12% Cr heat resistant steels. *Materials Letters* 63 (28), 2423 – 2425.
- Halama, R., Sedlak, J., Sofer, M., 2012. Phenomenological Modelling of Cyclic Plasticity.
- Hansen, N., Hughes, D. A., 1995. Analysis of large dislocation populations in deformed metals. *Physica Status Solidi (a)* 149 (1), 155–172.
- Higginson, R. L., Jepson, M. A. E., West, G. D., 2006. Use of ebsd to characterise high temperature oxides formed on low alloy and stainless steels. *Materials Science and Technology* 22 (11), 1325–1332.
- Holdsworth, S., Mazza, E., Binda, L., Ripamonti, L., 2007. Development of thermal fatigue damage in 1CrMoV rotor steel. *Nuclear Engineering and Design* 237 (24), 2292 – 2301.
- Huang, X., Morito, S., Hansen, N., Maki, T., 2012. Ultrafine structure and high strength in cold-rolled martensite. *Metallurgical and Materials Transactions A* 43, 3517–3531.
- Hyde, T. H., Chambers, A. C., 1992. Creep–fatigue crack growth in Jethete M152 at 550°C under mixed mode conditions. *The Journal of Strain Analysis for Engineering Design* 27 (1), 49–57.
- Jing, H., Luo, Z., Xu, L., Zhao, L., Han, Y., 2018. Low cycle fatigue behavior and microstructure evolution of a novel 9Cr–3W–3Co tempered martensitic steel at 650 °C. *Materials Science and Engineering: A* 731, 394 – 402.
- Jürgens, M., Olbricht, J., Fedelich, B., Skrotzki, B., 2019. Low cycle fatigue and relaxation performance of ferritic–martensitic grade P92 steel. *Metals* 9 (1), 99–124.
- Kitahara, H., Ueji, R., Tsuji, N., Minamino, Y., 2006. Crystallographic features of lath martensite in low-carbon steel. *Acta Materialia* 54, 1279–1288.

- Kupkovits, R. A., Neu, R. W., 2010. Thermomechanical fatigue of a directionally-solidified Ni-base superalloy: Smooth and cylindrically-notched specimens. *International Journal of Fatigue* 32 (8), 1330 – 1342.
- Li, H., Jing, H., Xu, L., Han, Y., Zhao, L., Rong, J., Tang, Z., Xiao, B., Zhang, Y., Luo, Z., Wu, D., 2019. Cyclic damage behavior of Sanicro 25 alloy at 700 °C: Dispersed damage and concentrated damage. *International Journal of Plasticity* 116, 91 – 117.
- Marahleh, G., Kheder, A., Hamad, H., 2006. Creep life prediction of service-exposed turbine blades. *Materials Science and Engineering: A* 433 (1), 305 – 309.
- Mishnev, R., Dudova, N., Kaibyshev, R., 2015. Low cycle fatigue behavior of a 10% Cr martensitic steel at 600°C. *ISIJ International* 55 (11), 2469–2476.
- O'Hara, E., Harrison, N., Polonski, B., Barrett, R., Leen, S., 2017. Fatigue damage characterisation of MarBN steel for high temperature flexible operating conditions. *Proceedings of the Institution of Mechanical Engineers, Part L: Journal of Materials: Design and Applications* 231 (1-2), 23–37.
- Perkins, K., Bache, M., 2005. The influence of inclusions on the fatigue performance of a low pressure turbine blade steel. *International Journal of Fatigue* 27 (6), 610 – 616.
- Rae, Y., Benaarbia, A., Hughes, J., Sun, W., 2019. Experimental characterisation and computational modelling of cyclic viscoplastic behaviour of turbine steel. *International Journal of Fatigue* 124, 581 – 594.
- Saad, A., Hyde, T., Sun, W., Hyde, C., Tanner, D., 2013. Characterization of viscoplasticity behaviour of P91 and P92 power plant steels. *International Journal of Pressure Vessels and Piping* 111, 246 – 252.
- Sauzay, M., 2009. Modelling of the evolution of micro-grain misorientations during creep of tempered martensite ferritic steels. *Materials Science and Engineering: A* 510-511, 74 – 80, 11th International Conference of Creep and Fracture of Engineering Materials and Structures, CREEP 2008.

- Sauzay, M., Brillet, H., Monnet, I., Mottot, M., Barcelo, F., Fournier, B., Pineau, A., 2005. Cyclically induced softening due to low-angle boundary annihilation in a martensitic steel. *Materials Science and Engineering: A* 400-401, 241 – 244, dislocations 2004.
- Sauzay, M., Fournier, B., Mottot, M., Pineau, A., Monnet, I., 2008. Cyclic softening of martensitic steels at high temperature—experiments and physically based modelling. *Materials Science and Engineering: A* 483-484, 410 – 414, 14th International Conference on the Strength of Materials.
- Seumangal, N., 2017. Influence of the heat treatment procedure on the stress corrosion cracking behaviour of low pressure turbine blade material FV566. Master's thesis, University of Cape Town.
- Smithells, C., 2013. *Metals Reference Book*. Elsevier Science.
- Turnbull, A., Zhou, S., 2011. Comparative evaluation of environment induced cracking of conventional and advanced steam turbine blade steels. Part 2: Corrosion fatigue. *Corrosion Science* 53 (1), 503 – 512.
- Wang, X., Zhang, W., Zhang, T., Gong, J., Abdel Wahab, M., 2019. A new empirical life prediction model for 9–12%Cr steels under low cycle fatigue and creep fatigue interaction loadings. *Metals* 9 (2).
- Zhang, S.-L., Xuan, F.-Z., 2017. Interaction of cyclic softening and stress relaxation of 9–12% Cr steel under strain-controlled fatigue-creep condition: Experimental and modeling. *International Journal of Plasticity* 98, 45 – 64.
- Zhang, Z., Hu, Z., Schmauder, S., 2016. Cyclic behaviour of 12% Cr ferritic-martensitic steel upon long-term on-site service in power plants. *Fatigue & Fracture of Engineering Materials & Structures* 39, 1179–1192.
- Zhao, P., Xuan, F.-Z., Wang, C., 2019. A physically-based model of cyclic responses for martensitic steels with the hierarchical lath structure under different loading modes. *Journal of the Mechanics and Physics of Solids* 124, 555 – 576.